



An improved heat transfer and fluid flow model of wire-arc additive manufacturing

W. Ou^a, G.L. Knapp^b, T. Mukherjee^b, Y. Wei^{a,*}, T. DebRoy^{b,*}

^a Department of Material Science and Technology, Nanjing University of Aeronautics and Astronautics, Jiangsu, 210016, China

^b Department of Materials Science and Engineering, The Pennsylvania State University, University Park, PA, 16802, USA



ARTICLE INFO

Article history:

Received 12 August 2020

Revised 12 November 2020

Accepted 15 December 2020

Keywords:

Heat transfer and fluid flow

Adaptive grid

Marangoni flow

Arc pressure

Droplet impact

H13 tool steel

Ti-6Al-4V

ABSTRACT

Wire-arc additive manufacturing provides the fastest metal printing rate among all printing processes. Heat transfer and fluid flow models offer a usable connection between process variables and the parameters that affect the structure and properties of parts. Here we develop a computationally efficient, three-dimensional, transient, heat transfer and fluid flow model to calculate temperature and velocity fields, deposit geometry, cooling rates, and solidification parameters that affect the microstructure, properties, and defect formation. Calculations are done for multi-track depositions of a tool steel H13 and a titanium alloy Ti-6Al-4V and the computed results are tested using experimental data for different processing conditions. It is found that convective flow and arc pressure are the two most important factors that govern the width and depth of penetration, respectively. An adaptive grid technique proposed here enhances the computational speed by as much as by 50% without affecting the accuracy of the computed results. For the same processing conditions, Ti-6Al-4V exhibits a larger fusion zone than that for H13 steel attributed to the lower density of Ti-6Al-4V. In addition, Ti-6Al-4V exhibits faster cooling rates during solidification than H13 steel because of the lower difference between the liquidus and solidus temperatures for Ti-6Al-4V. A smaller hatch spacing results in a larger pool and slower cooling rates during the solidification of both alloys.

© 2020 Elsevier Ltd. All rights reserved.

1. Introduction

Wire arc additive manufacturing (WAAM) is gaining attention because of its capability of producing large components rapidly [1–4]. However, several factors that govern the microstructure, properties, and defect formation in WAAM such as heat transfer, the flow of liquid metal in the molten pool, the evolution of 3D deposit geometry, and solidification are not well-understood [5,6]. Parts with desired microstructure and properties are fabricated by trial and error selection of various combinations of process variables including arc power, travel speed, wire diameter, wire feed rate, and hatch spacing [6]. In addition, the fabrication of a part by depositing multiple layers and hatches adds further complexity in the trial and error process [7].

A potential alternative to the trial and error approach is to calculate the most important variables that affect the microstructure, properties, and defect formation, such as temperature and velocity fields, deposit geometry, cooling rates and solidification parameters. Mechanistic models can provide these results and efforts have

been made to develop models based on phenomenological understanding. For example, a multi-layer analytical model was developed to predict deposit width and height [8]. However, this model did not explicitly calculate the heat transfer and fluid flow, and its accuracy may vary for different materials or processing conditions. Another analytical model [9] predicted the surface topology of multi-layer, multi-hatch structures with various hatch spacing using curve fitting. While the analytical models are computationally efficient for determining the bead shape, the effects of convective heat transfer are ignored, and the shape of the fusion zone and other important metallurgical factors are not always accurately simulated. Such models are easy to use and computationally efficient, but the limited physics considered in these models affects the accuracy of the results [1].

Numerical heat conduction models consider more complex physics than the analytical models and can be used to calculate three-dimensional, transient temperature distributions during WAAM. Heat conduction models have been shown to calculate approximate transient temperature fields for multiple layers of thin-wall deposition [10,11], but these models require the deposit shape to be known a priori. Furthermore, these models ignore the convective heat transfer within the molten pool which is often the

* Corresponding authors.

E-mail addresses: yhwei@nuaa.edu.cn (Y. Wei), debroy@psu.edu (T. DebRoy).

List of Symbols

A	Top-surface area of control volume
B	Small numerical constant (1e-10)
C	Carman-Kozeny coefficient
C_p	Specific heat
f_l	Liquid fraction
g	Gravitational acceleration
h	Specific sensible heat
h_c	Convection coefficient
H_d	Droplet heat content
ΔH	Latent heat of fusion of alloy
$\Delta H_{v,i}$	Latent heat of vaporization for element i
I	Arc current
J_h	Net surface heat flux
k	Thermal conductivity
M_i	Molecular mass of element i
p_i	Partial pressure of element i
P	Pressure field
P_A	Arc pressure term
P_d	Droplet pressure term
r_b	Radius of arc
S	Momentum equation source term
S_H	Enthalpy source term
S_c	Surface curvature
S_V	Droplet heat source
T	Temperature field
T_a	Ambient temperature
T_L	Liquidus temperature
T_S	Solidus temperature
T_ϕ	Surface temperature
\mathbf{u}	Velocity vector field
V	Volume of a control volume
V_a	Arc voltage
x_b, y_b	Cartesian distances to arc center
Δx_i	Length of control volume in dimension i
α	Accommodation coefficient
β	Volumetric thermal expansion
γ	Surface tension
$d\gamma/dT$	Surface tension temperature coefficient
ε	Emissivity
η	Arc efficiency
λ	Lagrangian parameter
μ	Viscosity
μ_m	Magnetic permeability
ρ	Density
σ	Stefan Boltzmann constant
σ_b	Standard deviation of arc current distribution
ϕ	Height function
ϕ_x, ϕ_y	1 st spatial derivatives of ϕ
$\phi_{xx}, \phi_{yy}, \phi_{xy}$	2 nd spatial derivatives of ϕ

dominant mechanism of heat transfer. Therefore, calculated temperatures and cooling rates are severely overestimated. Several researchers have simulated the process while considering heat transfer and fluid flow, but only for single-pass, multi-layer depositions [12,13] or multi-pass, single-layer depositions [14]. While these types of models can provide initial insights into the process, multi-pass, multi-layer models are needed for understanding the complex interactions between the shape of the previous deposit, heat buildup in the substrate/part, heat transfer, and fluid flow.

Simulation of multi-pass, multi-layer WAAM is computationally intensive. Numerical models that calculate the shape of the deposit generally utilize the volume of fluid (VOF) method which is com-

putationally challenging and can be a barrier to implementation of larger-scale calculations. A VOF model [13] was used for heat transfer and fluid flow calculations considering the surface tension and arc pressure as external forces. Another VOF model [14] accounted for the arc and droplet physics, including the effects of surface tension, arc pressure and arc shear stress effects on the surface. Though detailed, that investigation only considered two hatches of a single layer deposit. In addition, these VOF models are often inefficient for mass balance and may accumulate large errors in each time step during the calculation. The calculated time-lapse results are also difficult to compare with the experimental results.

Recently, we showed [15] the utility of the surface energy minimization method for calculating deposit geometry in WAAM considering arc pressure, droplet impact, heat transfer and fluid flow. The calculated deposit geometry and thermal cycle agreed well with the experimental results. However, the calculations were done only for a single-track deposit. Therefore, what is needed and currently not available is a computationally efficient, 3D, transient model of heat transfer and molten metal flow for multi-layer, multi-hatch WAAM that can provide 3D, curved deposit geometry by considering arc pressure, surface tension gradient driven fluid flow and droplet impact force as well as cooling rates and solidification parameters for different alloys and process conditions.

Here we develop and use a 3D, transient heat transfer and fluid flow model to calculate temperature and velocity fields, cooling rates, solidification parameters and the 3D deposit geometry during multi-track deposition WAAM process. The free surface profile of the 3D deposit was calculated by developing a transient implementation of a free surface energy minimization technique [3] that considers the surface pressure, arc pressure and droplet impact pressure. An adaptive grid system has been developed to achieve high computational efficiency while limiting memory requirements for the simulation of large transient problems in builds involving multiple layers and hatches. The calculations are done for multi-layer, multi-hatch builds of two commonly used alloys, H13 tool steel (H13) and Ti-6Al-4V. Experiments are performed at various processing conditions to rigorously test the computed results.

2. Numerical modeling of heat transfer and fluid flow

A 3D, transient heat transfer and fluid flow model is used to calculate temperature and velocity fields, fusion zone and deposit geometries, cooling rates and solidification parameters. This model expands upon previous works that used steady-state calculations [15–18], and the core numerical implementation based on the semi-implicit pressure linked equation (SIMPLE) method remains unchanged. The salient advancements are the changes to material properties assignment and coupling of the surface deformation calculation to the heat transfer and fluid flow solution.

The solution domain for heat transfer and fluid flow calculations consists of the substrate, shielding gas and multi-layer multi-hatch build as shown in Fig. 1. The scanning, hatching, and building directions are indicated by X, Y and Z, respectively. Unidirectional scanning strategy is used where the arc travels only along the positive X-direction for all layers and hatches. After a hatch is completed, the arc shifts along the positive Y-axis by a distance equal to the hatch spacing and returns to the starting location of the hatch on the X-axis. After the completion of all hatches in a layer, the arc shifts back to the initial position. A constant standoff distance of the electrode to the deposit surface is assumed. This repeats until all hatches and layers are completed.

The rest of this section focuses on the details of the special features of the new model. Symbols are defined in the list of symbols at the beginning of the paper. The assumptions made in the model are as follows:

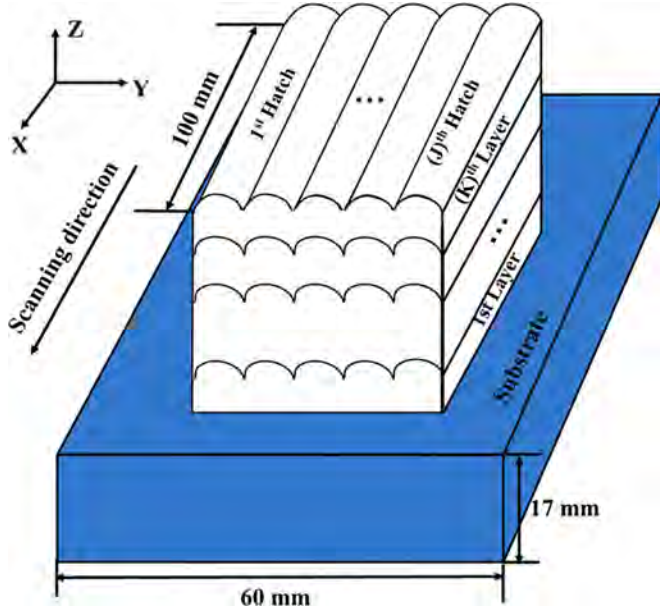


Fig. 1. Schematic of the solution domain consisting of substrate, shield gas and build. X, Y and Z directions represent the scanning, hatching and building directions, respectively. The J^{th} hatch represents the last hatch deposited along the Y direction, J can be any number the system permits, as well as the K^{th} layer is the last layer deposited along the Z direction. Width and height of the build vary depending on the process parameters mentioned in Table 3. However, all deposits are of a constant length of 100 mm. Unidirectional scanning strategy was used where all tracks are scanned in the same direction (along the positive X-axis).

- 1 Fluid flow is incompressible. Enhanced mixing due to turbulence of droplet impact and fluid flow is considered using uniform enhancement of thermal conductivity and viscosity [15,24].
- 2 Droplet parameters for the time-averaged heat source model are the same as droplet parameters from previous work [15–18] which used a similar machine and process parameters.
- 3 Recoil pressure due to vaporization is ignored, because surface temperature is significantly below the boiling point of the alloys.
- 4 Emissivity for black body radiation heat loss is independent of temperature.
- 5 Liquid material properties are independent of temperature.
- 6 Fluid flow in the mushy zone follows the Carman-Kozeny equation for fluid flow through a porous medium [1].
- 7 The arc power and arc pressure are assumed to have an exponential distribution around the arc axis.

2.1. Governing equations, heat sources and boundary conditions

The heat transfer and fluid flow model solved transient equations of conservations of mass, momentum and energy in three-dimensions. Governing equations were discretized on a Cartesian grid using a finite difference control volume method [19,20]. These discretized equations are then solved by the tri-diagonal matrix algorithm to obtain the enthalpy and velocity fields. The equation of momentum conservation in the 3D cartesian coordinate can be written as:

$$\rho \frac{\partial \mathbf{u}}{\partial t} + \rho(\nabla \cdot \mathbf{u}) = \nabla \cdot (\mu(\nabla \cdot \mathbf{u})) + S \quad (1)$$

The liquid metal is assumed to be a Newtonian fluid and viscosity of the liquid is taken to be constant [21]. The source term S includes pressure, frictional dissipation in the mushy zone [16], buoyancy force [17], and Marangoni forces for control volumes at

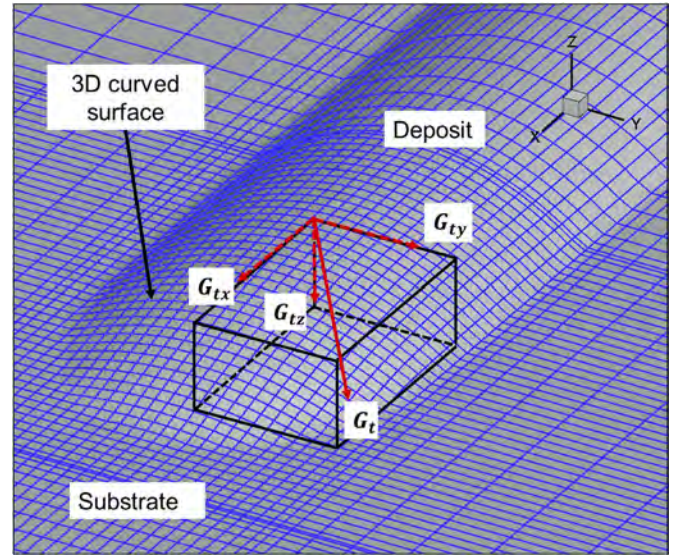


Fig. 2. The Marangoni stress tangents to the 3D curved surface in Cartesian coordinate system. \mathbf{G}_t represents the spatial temperature gradient vector at the molten pool surface, G_{tx} , G_{ty} and G_{tz} are the vector components along X, Y and Z axis, respectively.

the liquid-gas interface [22].

$$S = -\nabla P + \rho g \beta (T - T_L) - C \left[\frac{(1 - f_l)^2}{f_l^3 + B} \right] u_j + f_l \frac{d\gamma}{dT} (\mathbf{G}_t) \frac{\Delta x_i}{A_s} \quad (2)$$

The second, third, and fourth terms correspond to the buoyancy force, frictional dissipation in the mushy zone, and Marangoni force, respectively. Frictional dissipation in the mushy zone corresponds to the flow through a porous media according to the Carman-Kozeny equation [23] ($C = 1.6e11 \text{ N s m}^{-4}$). The liquid fraction f_l is one when temperature is greater than liquidus (T_l), zero when temperature is less than solidus (T_s), and varies linearly between zero and one for $T_s \leq T \leq T_l$. For Marangoni force, the components of spatial temperature gradient \mathbf{G}_t are taken along the liquid-gas interface as shown in Fig. 2. The Marangoni force term is only applied at control volumes at the surface of the molten pool and is zero elsewhere in the domain. The respective vector components of the temperature gradient are used as source terms for the calculation of u , v and w velocity components on the Cartesian grid.

The pressure field for an incompressible fluid is obtained by satisfying the continuity equation:

$$\rho \nabla \cdot \mathbf{u} = 0 \quad (3)$$

The energy conservation equation contains the latent heat source term, as well as a volumetric heat source/sink term that considers heat additions and losses from the deposit.

$$\rho \frac{\partial h}{\partial t} + \rho \nabla \cdot (\mathbf{u}h) = \nabla \cdot \left(\frac{k}{C_p} \nabla h \right) + S_H \quad (4)$$

$$S_H = -\frac{\partial(\rho u_i \Delta H)}{\partial x_i} + J_h \frac{A}{V} - \frac{\partial(f_l)}{\partial t} \Delta H_f + S_V \quad (5)$$

The first term in the right-hand side of Eq. (5) represents the heat release due to the change in enthalpy, the second is the net heat flux at the molten pool surface, the third is the latent heat of fusion, and the fourth is the heat from the droplet. The source term S_V is calculated assuming that the heat energy from the metal droplets is distributed uniformly in a cylindrical cavity [18]. This term is described in detail in our previous paper [15]. In this model, the molten pool surface is contained in the interior of

Table 1
Thermo-physical properties and droplet parameters of Ti-6Al-4V and H13 tool steel [36,37].

Properties	Ti-6Al-4V	H13
Liquidus temperature (K)	1928	1725
Solidus temperature (K)	1878	1585
Thermal conductivity (W/m K)	$1.57 + 1.6 \times 10^{-2}T - 1 \times 10^{-6}T^2$	$18.39 + 7.52 \times 10^{-3}T$
Specific heat (J/kg K)	$492.4 + 2.5 \times 10^{-2}T - 4.18 \times 10^{-6}T^2$	$394.8 + 0.2142T$
Liquid thermal conductivity (W/m K)	34.60	30.96
Liquid specific heat (J/kg K)	831.08	823.96
Latent heat of fusion (J/kg)	2.86×10^5	2.74×10^5
Density (kg/m ³)	4000	7800
Viscosity (kg/m s)	4.0×10^{-3}	5.7×10^{-3}
$d\gamma/dT$ (N/m K)	-0.26×10^{-3}	-0.43×10^{-3}
Arc efficiency	0.77	0.77
Wire radius (m)	0.6e-3	0.6e-3
Feeding rate (m/s)	86.7	64.9
Droplet radius (m)	0.3e-3 (estimated)	0.3e-3 (estimated)
Droplet velocity (m/s)	4.5 (estimated)	4.5 (estimated)

the domain with gas above it, and its location is tracked by height function ϕ (Section 2.2). Therefore, the heat flux at the deposit surface, J_h , is modified by A/V to convert from a flux to a volumetric source.

$$J_h = \frac{(IV_a\eta - H_d)}{2\pi r_b^2} \exp\left(-\frac{x^2 + y^2}{2r_b^2}\right) - \varepsilon\sigma(T_\phi^4 - T_a^4) - h_c(T_\phi - T_a) - \sum_{i=1}^N \alpha \Delta H_{v,i} p_i \sqrt{\frac{M_i}{T}} \quad (6)$$

On the right-hand side, the first through fifth terms correspond to the heat source from the arc [24], radiation heat loss, convection heat loss, and vaporization heat loss [25]. Convective heat loss considers $h_c = 8 \text{ W m}^{-2}$ at the liquid-gas and solid-gas interface to approximate natural convection by air and within the arc radius $h_c = 80 \text{ W m}^{-2}$ to approximate forced convection from the shielding gas based on typical values in literature [12,15]. Partial pressures of elements were calculated from the surface temperature and alloy composition using tabulated data [26] and the Clausius-Clapeyron relation [27] for temperatures outside tabulated ranges. Vaporization heat loss based on the Langmuir equation is modified by the accommodation coefficient, α , which accounts for recondensation of vapor on the surface and is approximated as 0.05 [28].

All specified source terms vary spatially. Detailed thermo-physical properties and droplet parameters of the H13 and Ti-6-Al-4V are listed in Table 1. Effective thermal conductivity and viscosity of the liquid metal are enhanced to account for turbulent convection effects [24,38]. The concepts of the enhancement factors were originally developed in the fusion welding literature [24,38] and have also been applied in additive manufacturing modeling [15]. The enhanced thermal conductivity and viscosity can vary between 5-10 times the nominal values depending on the local fluid flow conditions [38]. Here, an average property enhancement is applied over the entire melt pool with a thermal conductivity multiplier of 8 and viscosity multiplier of 10. The gas region is assumed to be stationary for solving the velocity and pressure fields.

Boundary conditions for the domain are specified separately for domain boundaries bordering the metal and gas regions. The entire domain is initialized at ambient temperature. The metal region has a boundary flux based on convective heat loss ($h_c = 8.4 \text{ W m}^{-2}$) and the gas region boundary temperature is held at T_a (298 K).

2.2. Calculation of the deposit geometry

The 3D curved surface of the deposit is calculated by using the free surface energy minimization method [15,16]. This method requires the initial local curvature of the liquid-gas interface, the pressures acting on that interface, and the spatially varying surface

tension. The molten pool surface deformation is constrained by the volume change of the surface needing to equal the volume added by wire feeding in each time step. The solution to the deformation of the surface considering all the aforementioned constraints is solved by the method of Lagrange multipliers, generating the following equation,

$$\rho g \phi = \lambda + P_A + P_d - 2\gamma S_k + \gamma \frac{(1 + \phi_y^2)\phi_{xx} - 2\phi_x\phi_y\phi_{xy} + (1 + \phi_x^2)\phi_{yy}}{(1 + \phi_x^2 + \phi_y^2)^{3/2}} \quad (7)$$

where P_A and P_d are defined as,

$$P_A = \frac{\mu_m \eta^2}{8\pi \sigma_b} \exp\left(-\frac{x_b^2 + y_b^2}{2\sigma_b^2}\right) \quad (8)$$

$$P_d = \frac{\rho V_d f_d}{\pi r_d^2} \exp\left(-\frac{2(x_b^2 + y_b^2)}{r_d^2}\right) \quad (9)$$

For this calculation, the volume addition rate from the wire is averaged over time rather than considering individual droplets. To solve the static force balance equation, Eq. (7) is discretized using Taylor series finite difference scheme [15,16]. Jacobi iterative method is used to solve the finite difference scheme. After guessing initial values λ , an iterative root-finding algorithm is used to find the correct value of the λ to satisfy the volume change constraint.

In Eq. (7), the second through fifth terms on the right-hand side terms correspond to the arc pressure [29], droplet impact pressure [30], Laplace pressure, and resistance to deformation of the surface, respectively. The fifth term is derived from the Young-Laplace equation [15,16], indicating the pressure needed to change the curvature of the surface. Since Young-Laplace equation is proposed under the static pressure condition, the discrete time step should be small enough to trace the dynamic free surface. The terms for surface tension, curvature, and distance from the arc source vary spatially. Surface curvature is calculated from the height function using the method of Lopez et al. [31]. The boundary conditions (Eq. 6) are applied on the cells nearest to the moving interface. At each time step boundary conditions are updated based on the current position of the interface. Therefore, the boundary conditions are updated continuously as the interface moves during the deposition process.

2.3. Adaptive mesh algorithm

A conventional fixed grid system requires fine grid resolution in anywhere that may have molten material in any time step of the

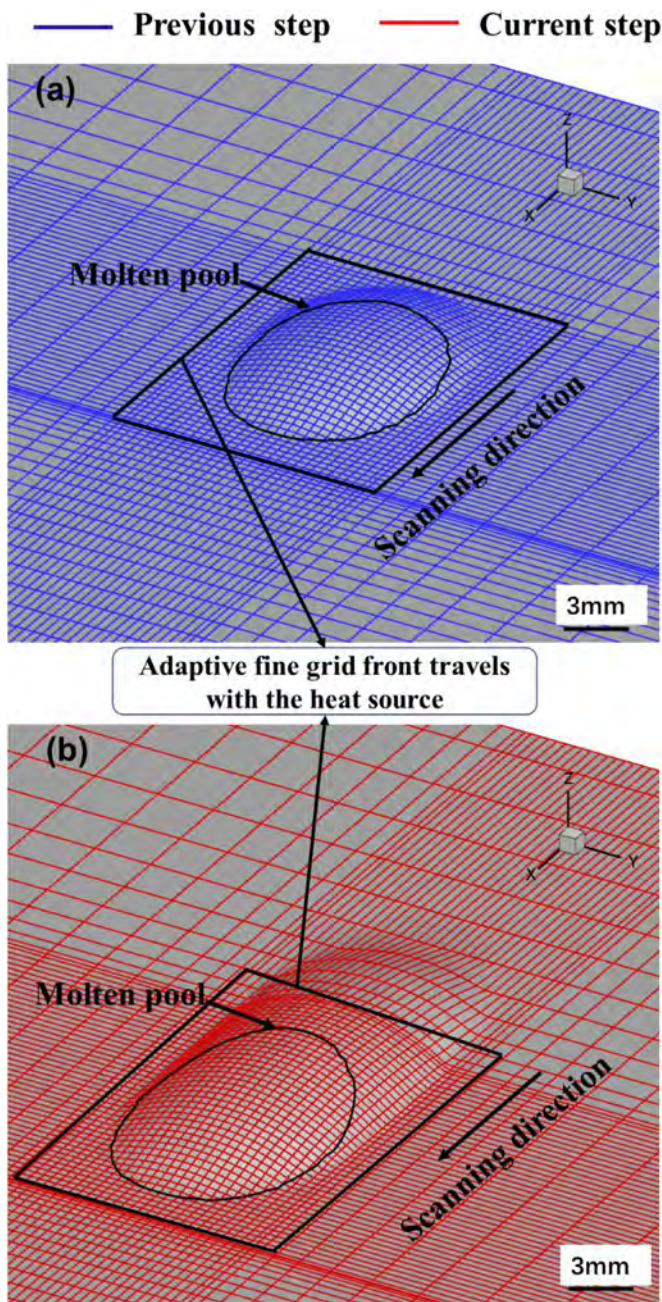


Fig. 3. The adaptive grid system on the top surface at (a) previous step and (b) current step. The molten pool profile is presented by the liquidus temperature of H13. The fine adaptive grid region travels with the heat source in such a way that it always contains the molten pool.

simulation. However, the molten pool is only present in a small portion of the domain at any given time step. Therefore, in most computational steps there is a large region of the domain that has fine grid resolution but no molten pool. Adaptive meshes have been applied in previous additive manufacturing simulations to alleviate this problem [19,32]. Here, an adaptive mesh scheme is used to ensure that the molten pool region is completely contained within a fine grid while the rest of the grid is coarser.

To generate a new mesh for a given time step, two factors are considered. First, the minimum size of the fine mesh region is such that it must fully contain the heat source. Second, the fine mesh must completely enclose all cells where $T > T_s$. Fig. 3(a-b) shows the grid update process between two consecutive time steps. The

grids only update in one dimension at a time. Also, the mesh spacing in the z-direction remains static. This speeds calculation by taking advantage of the structured *ijk*-ordering of the Cartesian mesh by allowing interpolation of entire planes of nodes (e.g., the *i*-plane if updating in the *x*-direction) rather than interpolating each node individually. Linear interpolation is used for generating the values of scalars on the new mesh from the values on the previous mesh.

An important consideration when implementing an adaptive mesh algorithm with interface tracking is that the height function must be stored on a persistent fine mesh. At the beginning of the simulation, a persistent fine mesh for the height function is generated. Any changes in height from a given time step are interpolated onto the persistent fine mesh. Surface height change occurs only on cells in the molten pool, so the adaptive mesh will always have a fine resolution in the regions where the height function changes. The persistent fine mesh height is then used to interpolate the height function of the adaptive mesh for the next time step.

2.4. Simulation details

The entire solution domain is divided into small control volumes. For a 100 mm long, 3-layer, 5-hatch structure, the total size of the solution domain is 150 mm × 82 mm × 47 mm (length × width × height). Convergence studies showed that fine-mesh size of 0.4 mm was adequate for fluid flow and deposit geometry calculations to converge. In the adaptive case, the number of grids was dynamic, but in a static mesh case the domain was 300 × 95 × 108 grids. The calculations are performed serially on a 2.2 GHz Intel Xeon Processor using an in-house Fortran code compiled using an Intel Fortran compiler. 800 time steps were solved for each pass. Details on simulation time are given in Section 4.1.

The residual value, or the error in the discretization of the governing equations, is used to judge if the convergence of the numerical solution. For the overall calculation domain, the residue value (*R*) is defined as:

$$R = \frac{\sum \left[\frac{1}{a_p} (a_e \Phi_e + a_w \Phi_w + a_n \Phi_n + a_s \Phi_s + a_t \Phi_t + a_b \Phi_b + f) - \Phi_p \right]}{\sum \Phi_p} \quad (10)$$

where the coefficients *a* and *f* are the discretization coefficients at a grid point, Σ denotes the summation over all grid points of the solution domain, Φ is the corresponding variable, i.e. enthalpy or velocity components. The velocities and enthalpy calculations are iterated to obtain lower residues and good convergence as shown in Fig. 4. A decrease in residue to below 1.0e-2 was considered for convergence of velocity and pressure fields and below 1.0e-5 for convergence of the specific enthalpy field.

3. Experiments

A series of 100 mm long, 5 hatches, 1 layer and 2 layers builds using H13 wire were deposited on a 250mm × 150mm × 4mm AISI 1040 steel substrate. The heat source of WAAM was a custom-designed Panasonic digital MIG/MAG welding power source, which was inverter controlled using direct current (DC) with output current range from DC 30 A to 350 A and output voltage range from DC 12 V to 31.2 V. The specimens were fabricated using a welding robot combined with control box, workbench and wire feed system. The 6-axis independent movements of the robot are programmed and controlled by a software-based control system. The torch was kept perpendicular to the substrate surface and the contact tip to workpiece distance was 10 mm. The deposited builds were shielded from oxidation by supplying high purity argon at a flow rate of 15 L/min. For simplicity, a unidirectional scanning

Table 2
The WAAM process variables used in experiments and simulations.

Sample No.	Layer No.	Hatch spacing (mm)	Current (A)	Voltage (V)	Travel Speed (mm/s)
1	1	4.67	150	23	6.7
2	1	5.44	150	23	6.7
3	1	6.22	150	23	6.7
4	2	4.67	150	23	6.7
5	2	5.44	150	23	6.7
6	2	6.22	150	23	6.7

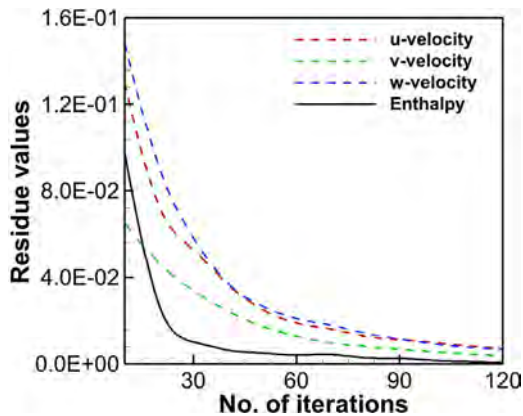


Fig. 4. Variations of calculated residues or error values with iterations for three components of velocity and enthalpy during calculation of H13 steel build with 6.7 mm/s scanning speed and 3450 W power.

strategy where the arc travels along the positive X-direction for all layers and hatches was used. The hatch spacing and layer number are set as experimental variables to investigate the multi-layer, multi-hatch deposition process. The detail process conditions used in these experiments are provided in Table 2. The samples were ground and polished using colloidal silica and subsequently were etched using the standard Keller's reagent (2.5mL HNO₃+1.5mL HCL+1mL HF+95 mL H₂O) for 20 seconds. An optical microscope was used to take the macrograph of cross sections magnified five times.

4. Results and discussions

4.1. Temperature and velocity fields

Fig. 5 shows the temperature and velocity fields during WAAM of a single-track H13 deposit calculated using the heat transfer and fluid flow model. Fig. 5(a) shows the temperature and velocity fields in a three-dimensional isometric view. The color bands represent the ranges of temperatures corresponding to the figure legend and the velocity of liquid metal within molten pool can be estimated by comparing their lengths with reference vector. The region bound by the liquidus isotherm (1725 K) represents the fusion zone, also referred to as the molten pool. The two-phase solid-liquid region, also known as the mushy zone is represented by the region bound by the solidus (1585 K) and liquidus isotherms. Fig. 5(b) shows the temperature and velocity fields on the top surface. Because of the moving heat source, an elliptical molten pool formed. The surface tension gradient is the dominant force to drive the liquid metal within molten pool, and the fluid flows from the center to the periphery of the molten pool due to surface tension decreasing with the increasing temperature. Fig. 5(c) shows the transverse view of the deposited track. Here, the molten deposited material forms a crown above the substrate, and the molten pool also melts a significant portion of the substrate material due to the

high heat input. Fig. 5(d) shows the longitudinal view at the mid-width of the deposit. The molten pool is significantly depressed by the arc pressure and droplet impact pressure. As the liquid metal is forced to the rear of the molten pool, the crown is built up before it solidifies. As seen in Fig. 5(a) and Fig. 5(d), the volume of molten metal directly beneath the arc axis is smaller than the volume of molten metal in the crown region.

The shape and size of the deposit shown in Fig. 6 are useful for verifying the model by comparing them with the corresponding experimental data. For example, Fig. 6 and Fig. 7 show the comparison of the calculated deposit geometry using corresponding experiment results from the literature for a single-track H13 [15] and Ti-6Al-4V [33]. In Fig. 6, a high heat input and wire feed rate created a deep penetration near the center of the fusion zone of the H13 deposit which is correctly captured by the model. In Fig. 7, deposit width and height decrease with heat source travel speed owing to the reduction in heat input. Both Figs. 6 and 7 show good agreement between the numerically calculated and the experimental data. Some minor deviations from the experiments could have been caused due to the several simplifying assumptions of the model. Overall, these validations provide confidence in using the model to investigate the roles of important process parameters on deposit shape and size, temperature and velocity fields, cooling rates and solidification parameters.

In addition to validating the model results against experiments, the results obtained using the adaptive mesh algorithm were also compared with the corresponding results using a conventional fixed grid. In the fixed grid, the total number of control volumes and the control volume size remain constant throughout the simulation, whereas the adaptive mesh algorithm updates the number and size of control volumes as described in Section 2.3. Fig. 8(a-b) show the calculated temperature and velocity fields near the molten pool of the 1st layer, 1st hatch both with and without the adaptive mesh. The differences in the peak temperature, and maximum values of three velocity components calculated with and without the adaptive mesh are provided in Table 4. Figures 8 (a-b) and Table 4 show that the temperatures, velocities, and deposit geometry calculated using the adaptive mesh are similar to those calculated using the fixed grid system (without the adaptive mesh). For example, the length of the mushy zone at the trailing edge of the molten pool calculated using the adaptive grid is only about 9% shorter than that calculated using the fixed grid. The simulation using the fixed grid takes a longer time. This is because fine grids are required for the entire calculation zone, which becomes computationally burdensome for large geometries and increases the computation time. In contrast, the same results can be obtained at a low computational time by using the adaptive grid. For example, Fig. 8(c) shows that for both Ti-6Al-4V and H13, calculations using the adaptive grid require much less calculation time for multi-track deposits.

As mentioned in Section 2 of this article, deposit shape and size are affected by arc pressure, droplet impact pressure and the convective flow of molten metal. Fig. 9 shows the relative influence of these factors on the deposit geometry for both H13 and Ti-6Al-4V using process parameters detailed in Table 3. To evaluate the rela-

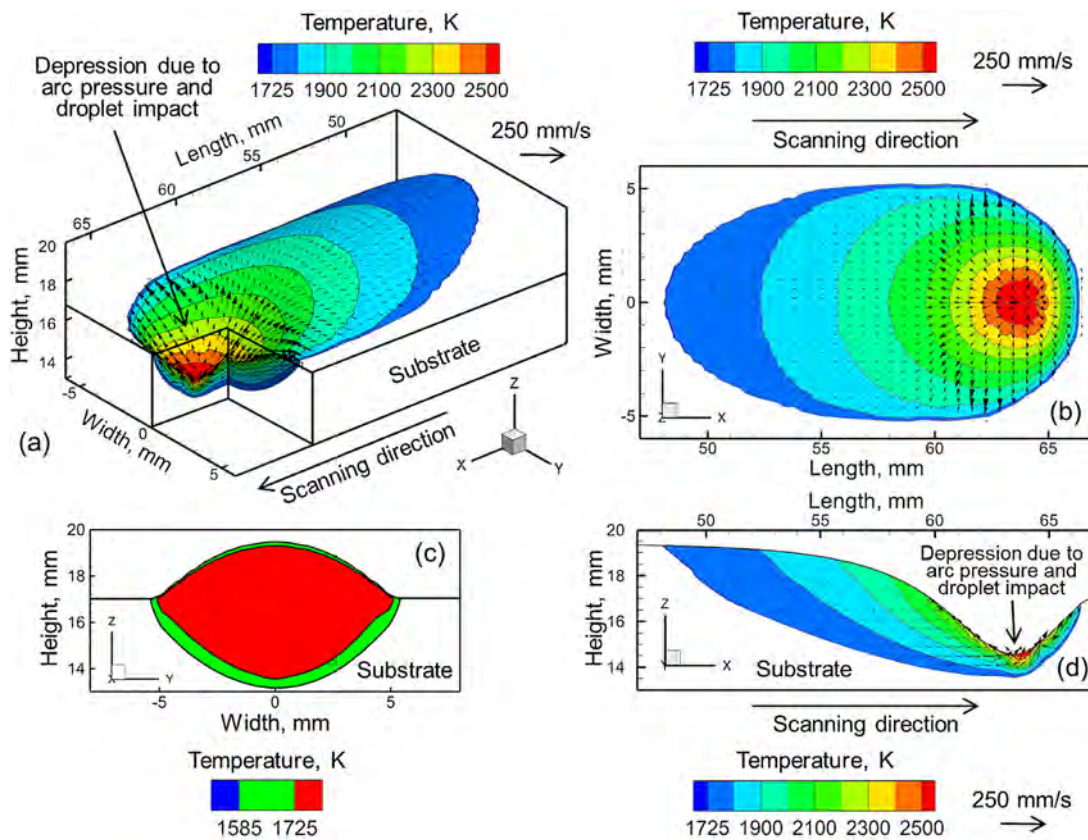


Fig. 5. The temperature profiles and velocity fields of H13 single-track deposition. (a) 3D isometric temperature field (b) top surface (c) transverse view and (d) longitudinal view. The scanning direction is along the positive 'X-axis'. The molten pool is extracted at $t=8.75$ s for a 120 mm, single-track deposit. At travel speed 5 mm/s, the x-location is 43.75 mm from the starting point. The process parameters using for simulation are given in Table 3.

Table 3

The WAAM process variables used in simulations. All simulations are for H13 alloy, except where indicated otherwise.

	Current(A)	Voltage(V)	TS(mm/s)	WFS(mm/s)	Hatchnumber	Layer number
Fig. 5	200	20	5.0	64.9	1	1
Fig. 6 (H13)	200	22	8.3	203.7	1	1
Fig. 7 (Ti64)	150	20	13.0	133.0	1	1
Fig. 8 (H13)	150	20	5.0	64.3	1	1
Fig. 8 (Ti64)	150	20	5.0	87.3	1	1
Fig. 9	200	20	6.7	132.0	1	1
Figs. 10–12	150	23	6.7	132.0	5	3
Fig. 13	150	23	6.7	132.0	5 (hs = 4.67–6.22mm)	1
Fig. 14	150	23	6.7	130.0	5 (hs = 4.67–6.22mm)	2
Fig. 15,17(H13)	150	23	6.7	132.0	2 (hs = 4.67–6.22mm)	2
Fig. 15,17(Ti64)	150	23	6.7	182.0	2 (hs = 4.67–6.22mm)	2
Fig. 16	150	23	6.7	132.0	2 (hs = 4.67–6.22mm)	2
Fig. 16(a) (H13)	200	20	5.0	64.9	1	1
Fig. 16(a) (Ti64)	200	20	5.0	86.7	1	1
Fig. 16(b)	150	23	6.7	130.0	5	2

itive influence, simulations were performed by including or excluding each of these factors. The simulations ignoring arc pressure and droplet impact force were performed by setting the corresponding source terms in Eq. (7) to zero. The simulation without the fluid flow solved only the energy conservation equation to calculate the temperature fields and deposit geometry, assuming the heat transfer only occurred by heat conduction. Fig. 9(a) shows H13 deposit height was decreased by 20% without arc pressure and 4% without droplet impact pressure. For Ti-6Al-4V, the height decreased by 25% and 3% without arc pressure and droplet impact pressure, respectively. Using only the heat conduction model (no fluid flow), the height increased by 22% for H13 and 2% for Ti-6Al-4V. Therefore, arc pressure is the most important factor that controls the

deposit height. This is primarily because of the arc's tendency to push the liquid metal to the back of the molten pool, behind the arc, which solidifies to form the elevated 3D shape of the deposit.

Fig. 9(b) shows that the H13 deposit width increased by 6% without arc pressure and increased by 1% without droplet impact pressure. For Ti-6Al-4V, the width increase was 8% without arc pressure and 1% without droplet impact pressure. The increase in deposit width without arc pressure corresponds with the reduced fluid flow to the rear end of the molten pool due to a lack of arc pressure. This results in hot liquid staying closer to the heat source and increasing the width of the deposit while decreasing the height. Calculation of the deposit width neglecting the fluid flow resulted in a 21% decrease for H13 steel and an 4% decrease

Table 4
The differences in the peak temperature, and maximum values of three velocity components calculated with the adaptive grid and static grid systems.

	Adaptive grid system	Static grid system	% difference
Peak temperature (K)	2951	2926	0.85%
U maximum (cm/s)	30.3	32.5	6.8%
V maximum (cm/s)	34.9	33.1	5.4%
W maximum (cm/s)	21.8	23.7	8.0%

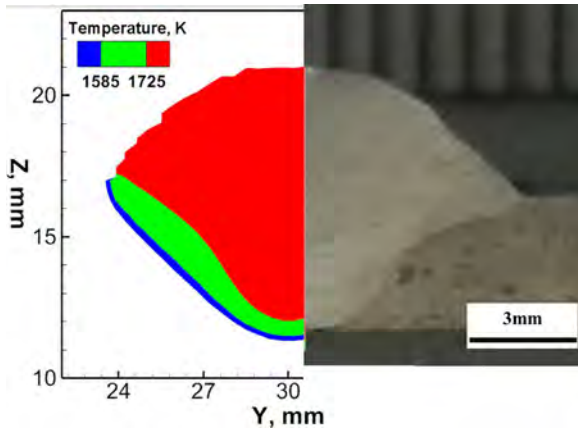


Fig. 6. Validation of deposit shapes and sizes for H13 Steel single-track deposit [15], with the simulation cross-section taken after 2.3 s of deposition. At travel speed 4.3 mm/s, the x-location is 9.89 mm from the starting position. Simulation parameters are given in Table 3.

for Ti6Al4V for the given process conditions, which indicates that for H13 fluid flow has the highest influence on deposit width. Arc pressure also plays an important role as it pushes material backwards and upwards, forming a higher and narrower deposit. Without as much material being pushed towards the back of the pool, the width of the deposit increases for both materials.

Though arc pressure and droplet impact pressure influence the geometry of the deposit, they do not significantly affect the peak temperature within the molten pool as evident from Fig. 9(c). The

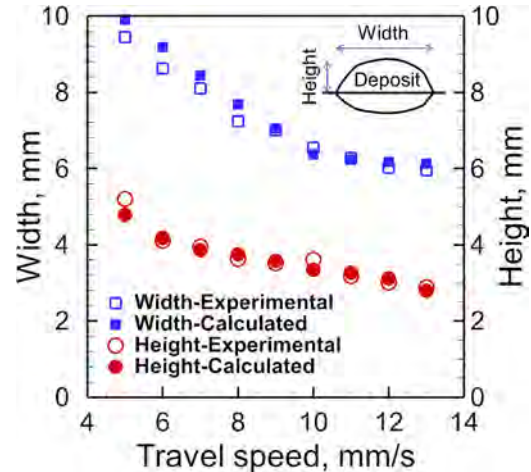


Fig. 7. Comparisons of the calculated deposit height and width with the corresponding experimental results [33] for Ti-6Al-4V single-track deposit at travel speeds varying from 5 mm/s to 13 mm/s. The deposit height and width are measured at the mid-length of the track from the transverse section indicated schematically in the inset. Simulation parameters are given in Table 3.

peak temperature is largely controlled by the ability of the liquid metal to transport heat away from the center of the pool through heat conduction and fluid flow. While the pressures acting on the surface dictate where the liquid metal flows, it does not change the amount of heat carried by the fluid as it is pulled away from the center of the molten pool. However, when the fluid flow is ignored, the peak temperatures at the monitored point in both materials

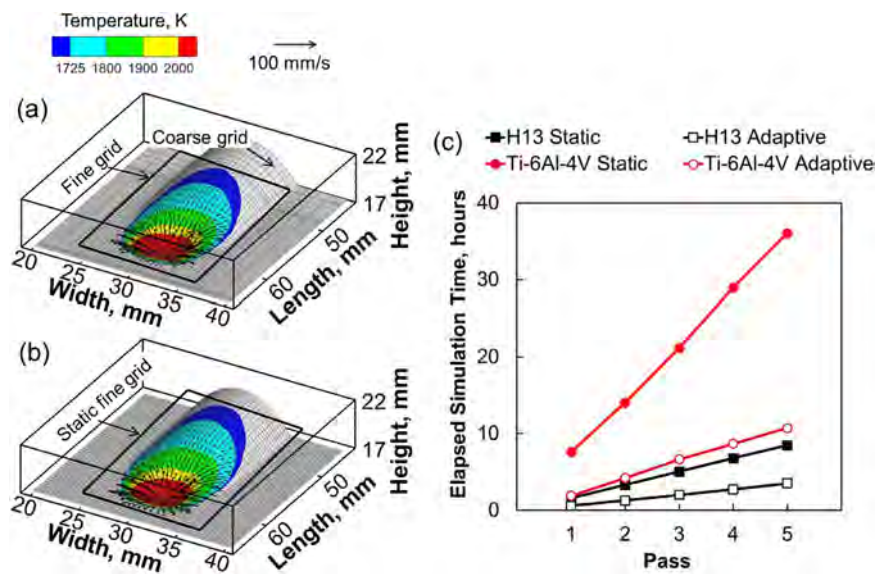


Fig. 8. (a) The calculated molten pool of first layer, first hatch of a H13 build using adaptive grid after 6.0 s of deposition. At travel speed 6.7 mm/s, the x-location is 40.2 mm from the starting position. (b) calculated molten pool using static grid at the same location as (a). The static grid is the grid system where the size of grid kept constant during simulation. (c) Simulation time for a 5-hatch, 1-layer H13 steel and Ti-6Al-4V titanium 10 cm long deposit using adaptive and static grid systems. Process parameters for the simulations can be found in Table 3.

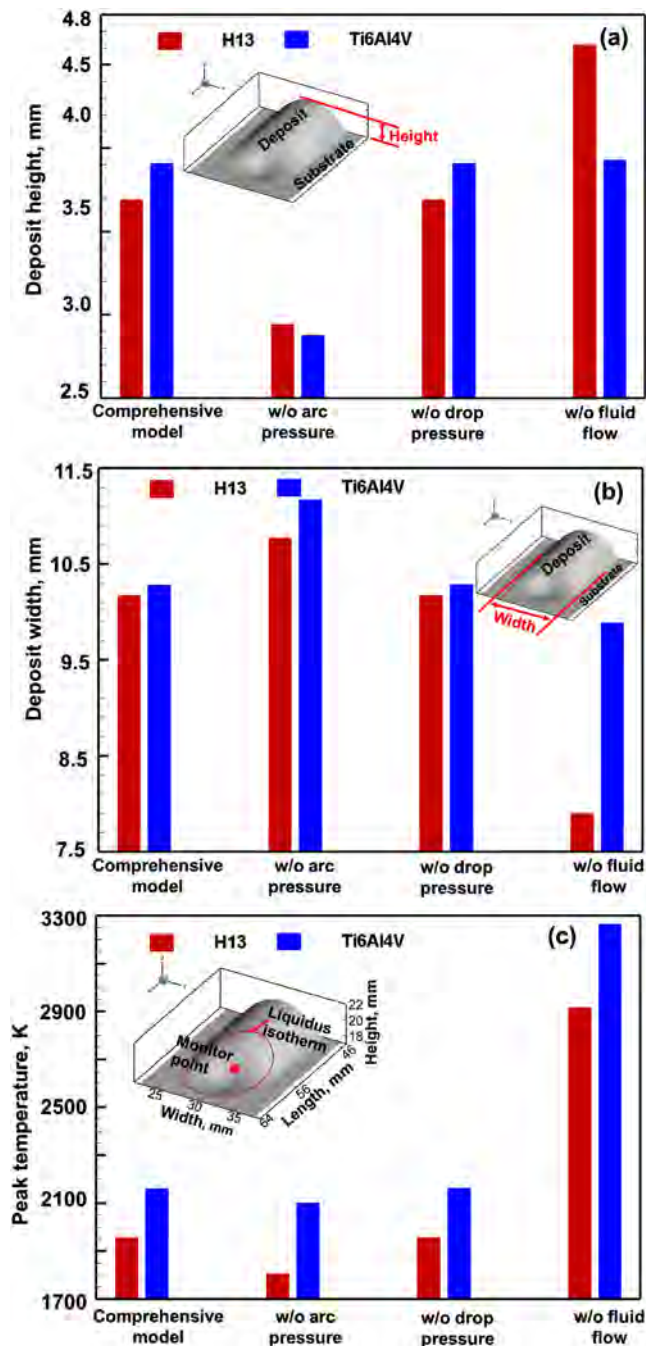


Fig. 9. The influence of different factors on the deposit geometry with the comprehensive model, without arc pressure model (w/o arc pressure), without droplet impact pressure model (w/o drop impact pressure), and without fluid flow model (w/o fluid flow). The comprehensive model is a rigorous model which considers the arc pressure, droplet impact pressure and fluid flow. (a) The calculated deposit height variation versus these different factors and (b) the calculated deposit width variation versus these different factors. (c) The calculated peak temperature variation at the specified monitoring point versus these different factors. Data was extracted after 7.5 s of deposition of a single-track simulation. At travel speed 5 mm/s, the x-location is 37.5 mm from the starting position. The process parameters are given in Table 3.

increase by about 1000 K, indicating that the fluid convection plays a significant role in transporting heat away from the molten pool and thus influencing the temperature distributions in the pool.

A well-recognized way of quantifying the impact of fluid flow on the heat transfer in the molten pool is to consider the dimensionless Peclet number (Pe). The Peclet number is a ratio of the

convective heat transfer due to fluid flow to heat transfer by thermal conduction and is defined as [34],

$$Pe = UL/\alpha \quad (11)$$

Here, L is the molten pool width, U is the maximum velocity, and α is the thermal diffusivity. When $Pe > 1$, fluid flow dominates the heat transfer mechanism inside the molten pool. For the comprehensive model in Fig. 9, the Peclet number is 268 for H13 and 135 for Ti-6Al-4V, both of which indicate that the fluid flow is a critical heat transfer mechanism inside the molten pool. As shown earlier in Fig. 9, the impact of fluid flow increased the molten pool width by 21% for H13 steel and 4% for Ti6Al4V and decreased the deposit height by 22% for H13 and 2% for Ti6Al4V. The higher Peclet number in the H13 molten pool correlates with a strong influence of fluid flow on the resultant deposit shape, whereas less of an influence on deposit shape was seen in Ti-6Al-4V which had a lower Peclet number in the molten pool. In previous research on the effect of process parameters on H13 steel, it was shown that a variation in wire feed rate of 10 mm s⁻¹ with similar process parameters yielded a 10% change in deposit height [15], so the impact of fluid flow on deposit geometry can vary significantly depending on the processing conditions.

4.2. Evolution of deposit geometry in multi-track deposition

The temperature and velocity distributions vary both spatially and temporally during multi-track depositions, because deposits form on top of the previously deposited tracks. To highlight the impact of previously deposited hatches and layers, Fig. 10, Fig. 11, and Fig. 12 explain the development of the deposit during a single hatch, across multiple hatches for a single layer, and over multiple layers, respectively.

Fig. 10 shows the progressive growth of the melt pool during a single-track deposition of H13. Fig. 10(a) schematically shows the three locations at the beginning, intermediate and end of the track for which the molten pools are shown in Figs. 10(b-d) respectively. At the beginning of the deposition, the molten pool exhibits a slightly elliptical shape and the depression on the top surface is not significant, as shown in Fig. 10(b). The arc pressure has a Gaussian distribution centered on the arc axis, so in a large molten pool the depression in the middle occurs due to a large arc pressure at the middle of the pool and lesser pressures at the side of the pool. However, in a small molten pool the arc pressure is comparatively homogeneous across the pool and less deformation occurs due to a smaller pressure differential across the surface. Fig. 10(c) shows that the molten pool gradually turns into a teardrop shape, which captures the effect of scanning along the positive x-axis. The molten material is pushed to the rear end of the fusion zone which solidifies to form the 3D deposit. Eventually, the molten pool reaches the steady state where the shape and size of the fusion zone do not vary with the progress of the deposition process as shown in Fig. 10(d). For a single-track deposition, the molten pool is symmetric because it was deposited on the flat substrate as shown in Fig. 10.

Fig. 11 shows the deposit shape varies with the deposition of multiple hatches. The shape and size of the fusion zones at three locations at the mid length of each hatch are compared. These three locations are schematically shown in Fig. 11 (a) as points 1, 2 and 3 for the 1st, 2nd and 3rd hatch respectively. Due to being built upon previously deposited material, the molten pool becomes asymmetric. This asymmetry comes from the uneven surface the material is being deposited onto and differences in temperature of the previously deposited material on one side and the shielding gas on the other. In Fig. 11(b-d), these temperature differences can be seen by looking at the asymmetric shape of the 1000 K and 1200 K isotherms. Heat accumulates in the previously deposited

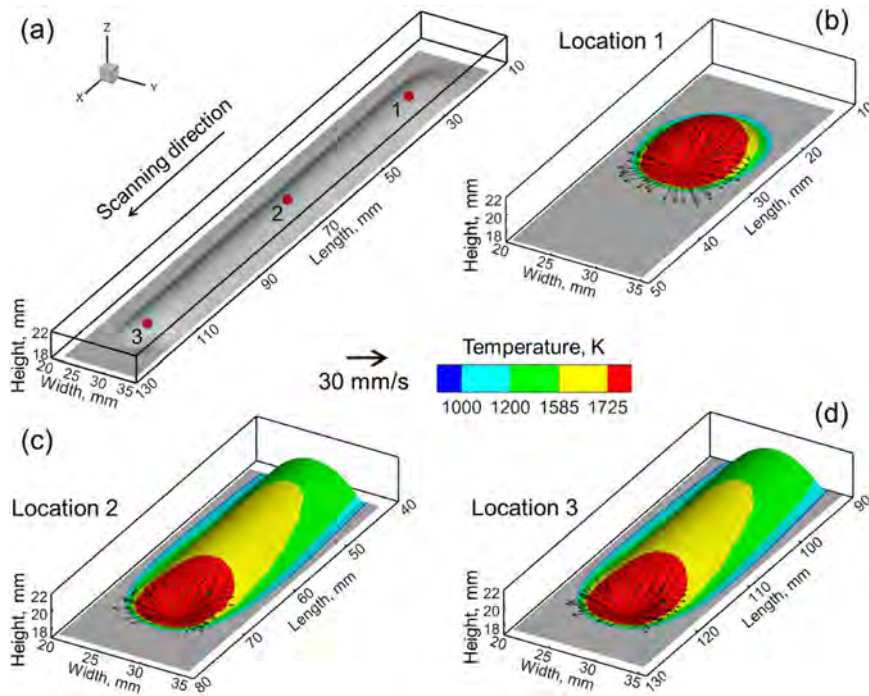


Fig. 10. (a) Schematic representation of a single-track deposit indicating three locations of the heat source axis 1, 2 and 3 for which fusion zones are shown in figures (b-d). Computed deposit shape, temperature field and velocity field of H13 build in 1st hatch 1st layer at (b) 10.05 mm from start location (location 1) (c) 50.25 mm from start location (location 2) (d) 100.5 mm from start location (location 3). The scanning direction is along positive 'X-axis'. The process parameters are given in Table 3.

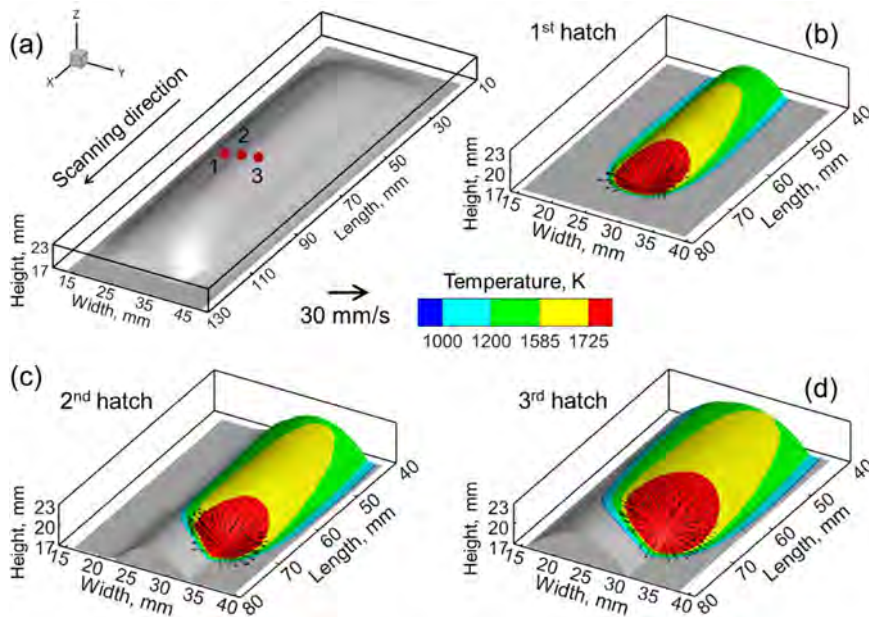


Fig. 11. (a) Schematic representation of a single layer, three hatches deposit indicating three locations of the heat source axis 1, 2 and 3 for the 1st, 2nd and 3rd hatches respectively at the mid-length of the track for which fusion zones are shown in figures (b-d). Computed deposit shape, temperature field and velocity field of H13 build in (b) 1st hatch 1st layer at 50.25 mm from start location (location 1) (c) 2nd hatch 1st layer at 50.25 mm from start location (location 2) (d) 3rd hatch 1st layer at 50.25 mm from start location (location 3). The scanning direction is along positive 'X-axis'. The process parameters are given in Table 3.

material during its deposition and deposition of the neighboring hatches more so than the substrate. The consequence of this asymmetry is that not only is material pushed backwards by the arc pressure and fluid flow, but it is also pushed back and over towards the larger area of the molten pool near the neighboring hatch. This causes material to go on top of the previously deposited material and deposit height to increase in sequential hatches, as shown in Fig. 11(b-d).

Fig. 12 shows the deposit and fusion zone shape and size at the mid length of each layer. The location 'A' in Fig. 12(a) schematically represents the location of the heat source axis for which fusion zones are shown for three different layers in Figs. 12(b-d). As the deposit height (layer number) increases, heat accumulates in the deposited material because the volume of the deposit increases while the contact area for conduction from the deposit into the substrate remains approximately constant. The

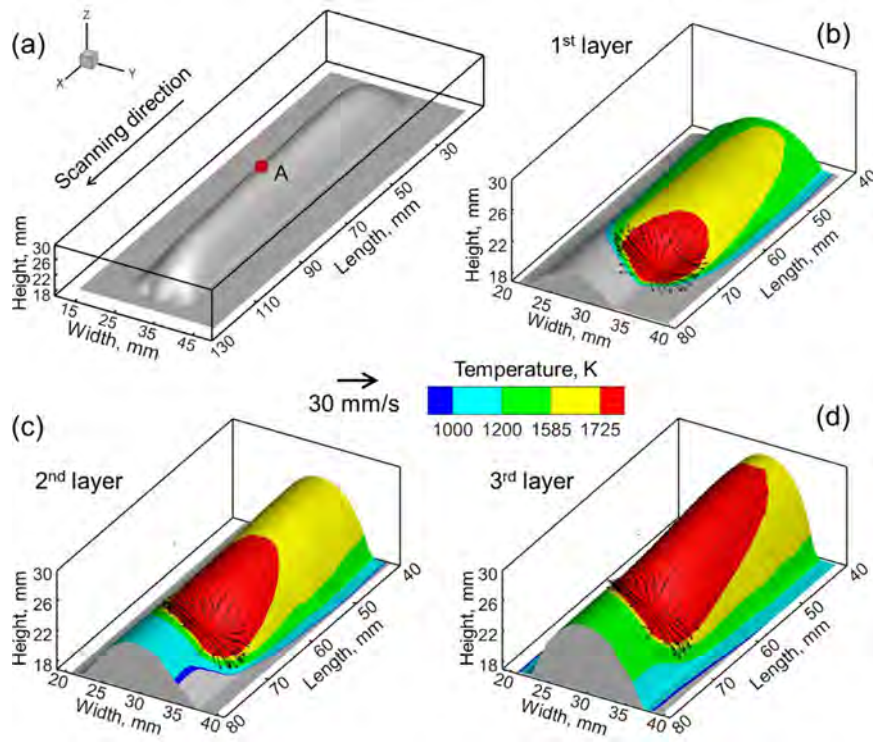


Fig. 12. (a) Schematic representation of a three layers, two hatches deposit indicating the location of the heat source axis A at the mid-length, mid width of 2nd hatch for which fusion zones are shown in figures (b-d) for three layers. Computed deposit shape, temperature field and velocity field of 2-hatch, 3-layer H13 build in (b) 2nd hatch 1st layer at 50.25 mm from start location (c) 2nd hatch 2nd layer at 50.25 mm from start location (d) 2nd hatch 3rd layer at 50.25 mm from start location. The scanning direction is along positive 'X-axis'. The process parameters are given in Table 3.

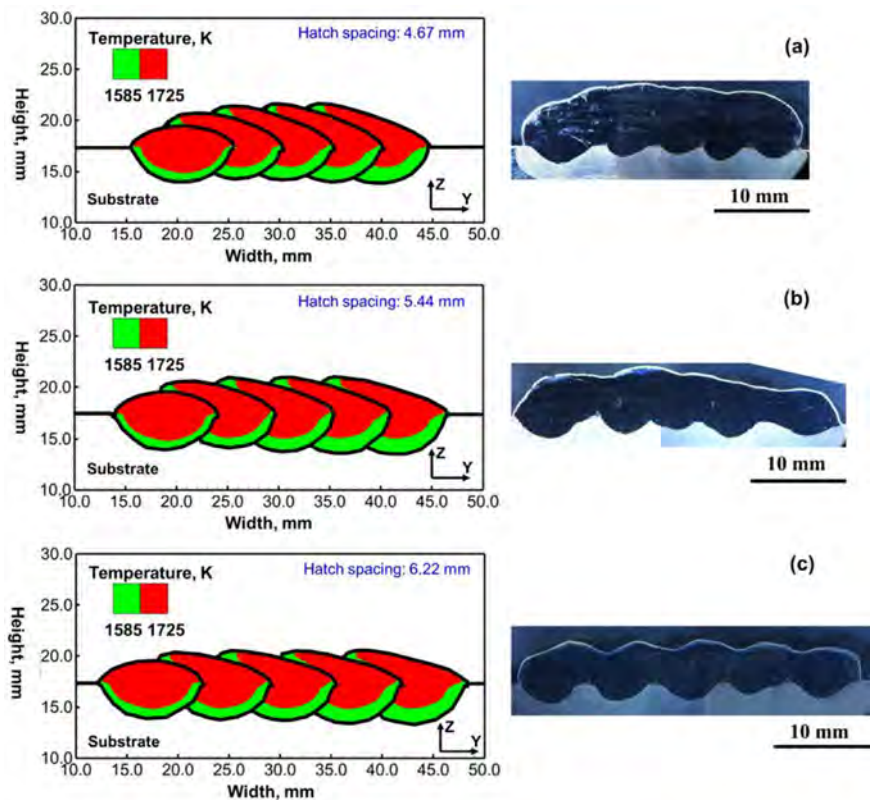


Fig. 13. Comparison between the calculated transverse sections at the position 50.25 mm from start location of the 5-hatch, 1-layer H13 deposit with the corresponding experimentally measured macrograph using (a) 4.67 mm (b) 5.44 mm and (c) 6.22 mm hatch spacing. Other process parameters are given in Table 3. The green region bounded by the solidus temperature (1585 K) isotherm represents the transverse section of the deposit. Hatching direction is along the positive 'Y-axis'.

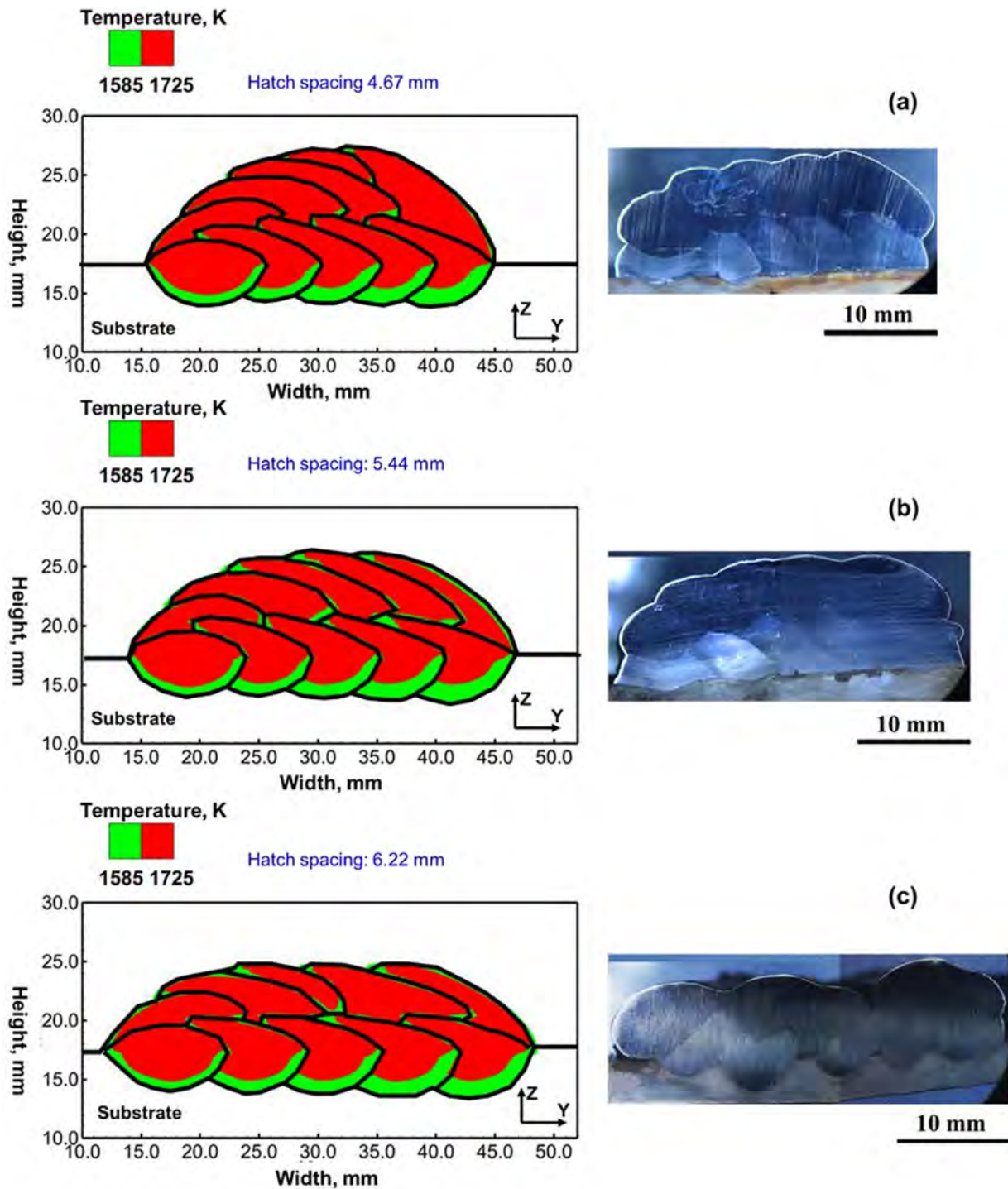


Fig. 14. Comparison between the calculated transverse sections at the position 50.25 mm from start location of the 5-hatch, 2-layer H13 deposit with the corresponding experimentally measured macrograph using (a) 4.67 mm (b) 5.44 mm and (c) 6.22 mm hatch spacing. Other process parameters are given in Table 3. The green region bounded by the solidus temperature (1585 K) isotherm represents the transverse section of the deposit. Hatching direction is along the positive 'Y-axis'.

molten pool volume, length, and width all increase with the deposit height which is generally undesirable for a controlled deposition process. One recourse is to increase the idle time between individual hatches and layers to allow time for the build to cool off. Also, because the second- and third-layer deposits are built upon already deformed layers, molten pool surfaces are inclined and asymmetric with respect to the axis of the heat source as shown in Fig. 12(b-d). Similar to the variation in deposit shape with hatch, asymmetry in the molten pool affects

where liquid metal flows in the molten pool and influences deposit shape.

Because the shape of previously deposited material affects the heat transfer and fluid flow in subsequent hatches and layers, the hatch spacing plays an important role in determining the geometry of the deposits. To examine the role of hatch spacing on deposit geometry and further validate the model, simulation results for various hatch spacings were compared to the corresponding experimental data. In Fig. 13, a comparison is made between the

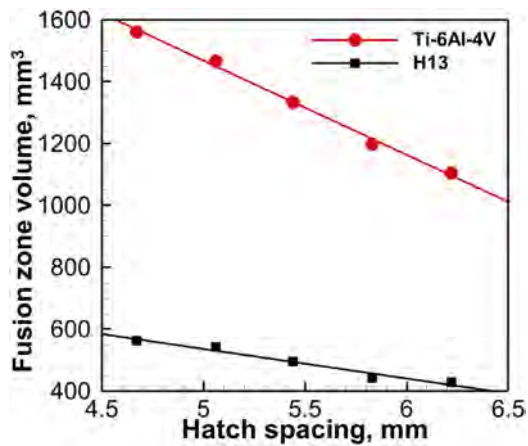


Fig. 15. Variation of fusion zone volume with hatch spacing for H13 and Ti-6Al-4V. Fusion zone is the region bound by the liquidus isotherm of the alloy and contains liquid material. The fusion zone volume was taken from the simulation halfway through the 2nd layer, 2nd hatch deposition. The process parameters are given in Table 3.

simulated fusion zone geometry of a single layer, five-hatch deposit built with three different hatch spacings and the corresponding build transverse cross-sections. The fusion zones for the 2nd to 5th hatch appear tilted with respect to the heat source axis because the molten droplet spreads over the previously deposited track. The main difference between the simulations and experiments is the penetration depth of the molten pool. This is likely a consequence of having to use assumed droplet parameters due to unavailability of experimentally measured droplet parameters for this particular material and process parameter combination. In this case, approximation of the droplet parameters overpredicted the depth of the fusion zone in the results calculated by the numerical model.

Continuing the examination of the effect of hatch spacing on geometry to multi-layer builds, Fig. 14 shows a fair agreement between the computed and the corresponding measured build shapes and sizes for 5-hatch, 2-layer H13 build. Deposited on the 3D curved surface of the first layer, the second layer deposit tends to have larger molten pool due to accumulated heat in the substrate and previously deposited material. There is a small mismatch between the simulated and calculated shape of the deposits on the first and last pass of the second layer. The overflow of the pool onto previous layers at the edges of the deposit (exemplified in the left-hand side Fig. 14c) may be the source of this mismatch. In addition, several simplified assumptions to make calculations tractable may also contribute to some discrepancy between the experimental and calculated results.

It is evident from Fig. 13 and 14 that the hatch spacing significantly affects the deposit shape and size. Fig. 15 shows the variations in fusion zone volume with hatch spacing for both H13 and Ti-6Al-4V. For both alloys, the fusion zone volume decreases with increasing hatch spacing. A smaller hatch spacing increases the overlap between the molten pool and the previously deposited track. In the case where the previous track is still hot, this reduces the heat flow away from the molten pool and results in a larger fusion zone. Ti-6Al-4V has a lower density than H13 which results in a larger fusion zone than that for H13 for the same processing conditions. It is evident that deposition of multiple layers and hatches with different hatch spacing significantly affect the temperature distributions and fusion zone geometry. The variations in temperature fields and fusion zone geometry also contribute to a wide variety of cooling rates and solidification parameters as described in the next section.

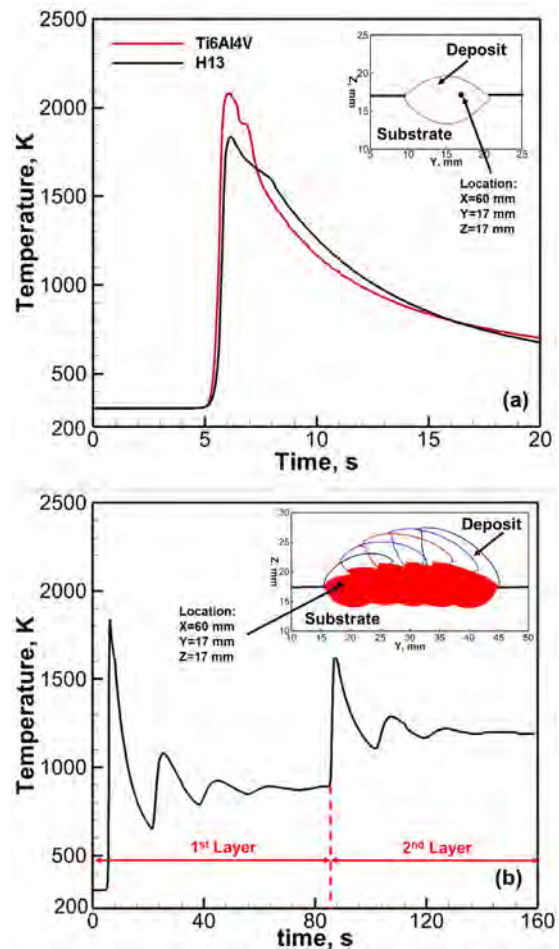


Fig. 16. (a) The thermal cycles of Ti-6Al-4V and H13 single-track deposit. (b) The thermal cycles of 5-hatch 2-layer H13 steel deposit. The location of monitor point is indicated by the inset schematic. The process parameters are given in Table 3. For X, Y and Z directions refer to Figure 1.

4.3. Cooling rates and solidification parameters

It is well understood that the temperature gradient, G , and the growth rate of the solidification front, R , provide important information about the solidification morphology and the scale of microstructure. Both can be derived from the transient temperature fields and can provide understanding of the conditions that govern the liquid-solid phase change. The product of G and R , GR , represents the cooling rate, which largely determines the scale of the microstructure. Also, the ratio G/R can provide information indicating the solidification morphology.

Both cooling rate and solidification parameters are affected by the transient variation in temperature during deposition, also known as thermal cycle, which can be calculated using the heat transfer fluid flow model. For example, thermal cycles for the depositions of Ti-6Al-4V and H13 steel are shown in Fig. 16. In Fig. 16(a), the thermal cycle for a monitoring point within a single hatch is shown. As the arc approaches the monitoring point in the first hatch of the first layer, the temperature rapidly increases to a peak temperature, and then the material cools and eventually solidifies. During the solidification from liquidus to solidus temperature latent heat release slows the cooling rate, corresponding with a change in the slope of the cooling curve. When the material is liquid, both the peak temperature and cooling rate depend on the thermo-physical properties of the material and the process parameters. Comparing the thermophysical properties of liquid Ti-

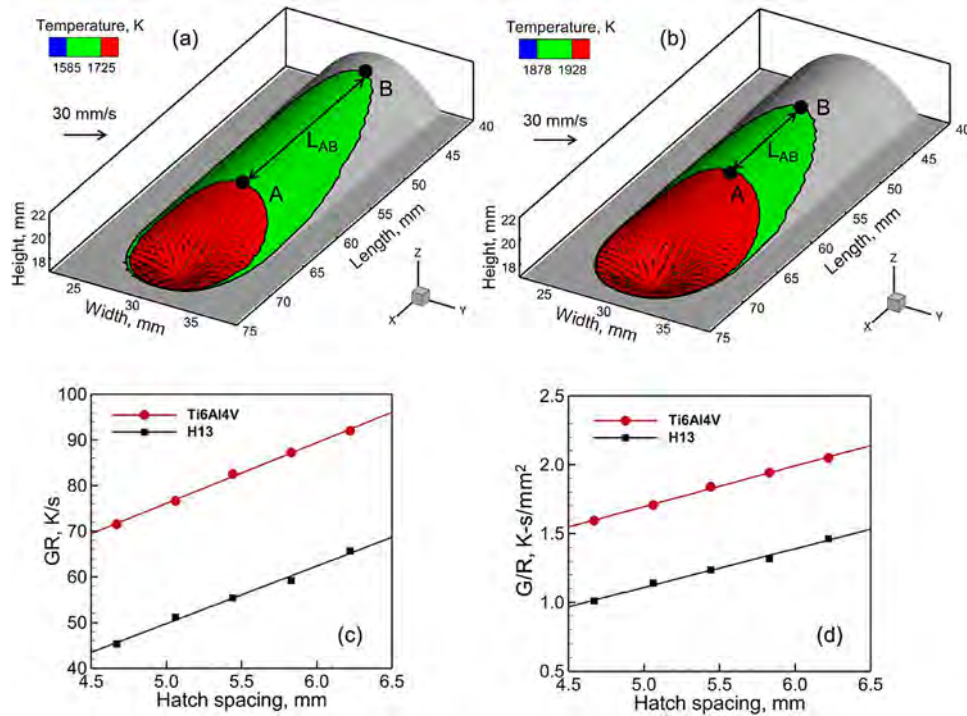


Fig. 17. 3D, isometric view of the molten pool for (a) H13 and (b) Ti-6Al-4V. 'A' is a point on liquidus isotherm, 'B' is a point on solidus isotherm. Both points are on the top surface and at the trailing edge of the molten pool. L_{AB} which is the distance between the two points 'A' and 'B' is used to calculate the temperature gradient between the liquidus and solidus isotherms. For both figures (a) and (b), the scanning direction is along the positive x-axis. (c) The cooling rate between liquidus temperature and solidus temperature variation with hatch spacing for 5-hatch 2-layer deposit of Ti-6Al-4V titanium and H13 steel. (d) The solidification parameters variation with hatch spacing for 5-hatch 2-layer deposit of Ti-6Al-4V titanium and H13 steel. The temperature gradient was calculated for all cases during the 1st layer, 2nd hatch at 60.3 mm from start location. The process parameters are given in Table 3.

6Al-4V and H13 provided in Table 1, both liquids have similar values of specific heat but Ti-6Al-4V has a much lower density. This means that once melted, the same amount of input energy will heat the Ti-6Al-4V melt faster and lead to a higher peak temperature, as shown in Fig. 16(a). For the same reason, the Ti-6Al-4V molten pool cools and solidifies more quickly than H13 for the same amount of heat dissipating from the pool. Faster solidification in Ti-6Al-4V is enhanced by the liquid having a higher thermal diffusivity than liquid H13, which indicates heat will dissipate more quickly from the Ti-6Al-4V molten pool once the heat source is removed.

In a multi-hatch, multi-layer deposition, each point experiences several heating and cooling processes. These complex thermal cycles during a two-layer, five-hatch H13 deposition are shown in Fig. 16(b) for a fixed point in the first hatch of the first layer. The first hatch of the first layer is similar to Fig. 16(a), with the material melting as the heat source approaches, then solidifying and cooling. In subsequent hatches on the first layer, the temperature rises as the heat source approaches the same x-axis location of the monitoring point, i.e., the same distance along the hatch. The peak temperature during subsequent hatches decreases as the hatches get farther away. Importantly, once the fifth hatch of the first layer is complete ($t \approx 80$ s), significant heating of the substrate and deposit has occurred, as the temperature plateaus around 900 K and only cools off slowly during the interlayer cooling time. Consequently, the temperatures during the second layer deposition are higher on average due to a substrate temperature that is effectively higher. By the end of the second layer, the temperature at the monitoring point is approximately 1200 K, showing significant heating has occurred and further explaining the trends of how pool size varies with layer described in Fig. 12. Due to the difficulty of measuring these temperature cycles *in situ*, a reliable numeri-

cal model is an effective method to estimate the spatially variation of cooling rates and solidification parameters for WAAM processes.

The temperature gradient (G) between liquidus and solidus temperature affects the driving force for heat transfer at the solidification front and can be used to calculate the cooling rate during solidification. G can be calculated as,

$$G = \frac{T_l - T_s}{L_{AB}} \tag{12}$$

where T_l is liquidus temperature, T_s is solidus temperature and L_{AB} is the distance between the locations of the liquidus temperature and solidus temperature. Here, L_{AB} is measured from the simulations at the mid-width of the molten pool along the top surface. This is shown in Fig. 17(a) and (b) for H13 tool steel and Ti-6Al-4V respectively. For Ti-6Al-4V, the temperature difference between liquidus and solidus temperature is 50 K, much smaller than the 140K difference for H13. Hence, L_{AB} of Ti-6Al-4V molten pool is much shorter, so the Ti-6Al-4V molten pool has a higher temperature gradient at the solidification front. For the same heat input of 514 J/mm, the L_{AB} was 4.7 mm for Ti-6Al-4V, but 20.7 mm for H13.

The growth rate of the solidification front, R , at the top surface of the molten pool along the centerline is equivalent to the scanning speed. Therefore, the higher temperature gradient at the solidification front in Ti-6Al-4V corresponds to a faster cooling rate during solidification than H13, as shown in Fig. 17(c). As evident from Fig. 15, larger hatch spacing results in smaller pool which solidifies faster. Therefore, cooling rate during solidification increases with the hatch spacing. For a constant travel speed, the G/R exhibits the same regular variation with hatch spacing as cooling rate, shown in Fig. 17(d). The low value of G/R in multi-layer, multi-hatch deposit indicates the liquid ahead of the solidifica-

tion will be supercooled and unstable plane front solidification will occur [15,35]. That is to say, the solidification morphology will be dendritic or cellular, which is typical of additive manufacturing. These results indicate that variations in cooling rate with hatch spacing could affect the solidification microstructure. However, the solidification front tends to deviate from plane front due to low values of G/R , so dendritic or cellular solidification will occur throughout the build regardless of the hatch spacing or process parameter changes.

5. Summary and conclusions

A computationally efficient numerical heat transfer and fluid flow model is developed to calculate the temperature and velocity fields, build geometry, cooling rates and solidification parameters for wire-arc additive manufacturing. Computed results are tested against experimental data for the deposition of H13 tool steel and Ti-6Al-4V alloys. Below are specific findings.

- (1) Fluid flow inside the molten pool significantly affects the geometry of the fusion zone. For example, calculations neglecting the fluid flow resulted in an 21% and 4% decrease in the predicted deposit width for H13 tool steel and Ti-6Al-4V, respectively, under the process conditions used here. The importance of the fluid flow on heat transfer is consistent with the calculated high values of Peclet numbers of 268 for H13 tool steel and 135 for Ti-6Al-4V, both of which indicate that the convective flow is a dominant heat transfer mechanism inside the molten pool.
- (2) Arc pressure is found to be the most influential factor controlling the deposit height when compared to the other important factors of droplet impact force and Marangoni force. This is due to the arc's tendency to push the liquid metal to the back of the molten pool which solidifies to form the 3D shape of the deposit. Calculations neglecting the arc pressure resulted in about 20% decrease in the predicted deposit height for both H13 tool steel and Ti-6Al-4V under the process conditions used here.
- (3) For the same processing conditions, Ti-6Al-4V exhibits a larger fusion zone than that for H13 tool steel. This is attributed to the lower density of Ti-6Al-4V than that for H13 tool steel. However, H13 exhibits a larger mushy zone than that of Ti-6Al-4V owing to the larger difference between the liquidus and solidus temperature of H13. Larger mushy zone in H13 results in lower temperature gradients and cooling rates during solidification than Ti-6Al-4V.
- (4) Use of an adaptive grid algorithm significantly enhances the computational efficiency without affecting the calculation accuracy. Comparing with a conventional fixed grid, the adaptive grid reduced the total calculation time by more than 50% because fine grids could be used only near the heat source where the spatial variation of temperature and other variables were maximum. The use of the adaptive grid allowed simulation of multi-layer, multi-hatch WAAM process in a computationally efficient manner.
- (5) A smaller hatch spacing increased the overlap between the molten pool and the previously deposited track. In cases where the previously deposited tracks were still hot, the heat flow away from the molten pool was reduced. Therefore, a smaller hatch spacing resulted in a larger molten pool for both H13 tool steel and Ti-6Al-4V. Since larger molten pools cool and solidify slowly, cooling rate during solidification decreased at smaller hatch spacing.

Declaration of Competing Interest

The authors declare that they have no known competing financial interests or personal relationships that could have appeared to influence the work reported in this paper.

CRediT authorship contribution statement

W. Ou: Methodology, Writing - original draft, Software, Validation. **G.L. Knapp:** Methodology, Writing - original draft, Software, Validation. **T. Mukherjee:** Conceptualization, Software, Investigation, Writing - original draft. **Y. Wei:** Investigation, Writing - review & editing, Supervision. **T. DebRoy:** Conceptualization, Supervision, Writing - review & editing.

Acknowledgements

The authors gratefully acknowledge a project funded by the Priority Academic Program Development of Jiangsu Higher Education Institutions (PAPD). Computations for this research were performed on the Pennsylvania State University's Institute for Computational and Data Sciences Advanced CyberInfrastructure (ICDS-ACI).

References

- [1] T. DebRoy, H.L. Wei, J.S. Zuback, T. Mukherjee, J.W. Elmer, J.O. Milewski, A.M. Beese, A. Wilson-Heid, A. De, W. Zhang, Additive manufacturing of metallic components—process, structure and properties, *Progress in Materials Science* 92 (2018) 112–224, doi:[10.1016/j.pmatsci.2017.10.001](https://doi.org/10.1016/j.pmatsci.2017.10.001).
- [2] T. DebRoy, T. Mukherjee, J.O. Milewski, J.W. Elmer, B. Ribic, J.J. Blecher, W. Zhang, Scientific, technological and economic issues in metal printing and their solutions, *Nature Materials* 18 (2019) 1026–1032, doi:[10.1038/s41563-019-0408-2](https://doi.org/10.1038/s41563-019-0408-2).
- [3] Q. Wu, T. Mukherjee, C. Liu, J. Lu, T. DebRoy, Residual stresses and distortion in the patterned printing of titanium and nickel alloys, *Additive Manufacturing* 29 (2019) 100808, doi:[10.1016/j.addma.2019.100808](https://doi.org/10.1016/j.addma.2019.100808).
- [4] T. DebRoy, T. Mukherjee, H.L. Wei, J.W. Elmer, J.O. Milewski, Metallurgy, mechanistic models and machine learning in metal printing, *Nature Reviews Materials* (2020), doi:[10.1038/s41578-020-00236-1](https://doi.org/10.1038/s41578-020-00236-1).
- [5] T. Mukherjee, T. DebRoy, Printability of 316 stainless steel, *Science and Technology of Welding and Joining* 24 (5) (2019) 412–419, doi:[10.1080/13621718.2019.1607061](https://doi.org/10.1080/13621718.2019.1607061).
- [6] H.L. Wei, T. Mukherjee, W. Zhang, J.S. Zuback, G.L. Knapp, A. De, T. DebRoy, Mechanistic models for additive manufacturing of metallic components, *Progress in Materials Science* (2020), doi:[10.1016/j.pmatsci.2020.100703](https://doi.org/10.1016/j.pmatsci.2020.100703).
- [7] J. Xiong, G. Zhang, H. Gao, L. Wu, Modeling of bead section profile and overlapping beads with experimental validation for robotic GMAW-based rapid manufacturing, *Robotics and Computer-Integrated Manufacturing* 29 (2) (2013) 417–423, doi:[10.1016/j.rcim.2012.09.011](https://doi.org/10.1016/j.rcim.2012.09.011).
- [8] S. Ríos, P.A. Colegrove, F. Martina, S.W. Williams, Analytical process model for wire+ arc additive manufacturing, *Additive Manufacturing* 21 (2018) 651–657, doi:[10.1016/j.addma.2018.04.003](https://doi.org/10.1016/j.addma.2018.04.003).
- [9] D. Ding, Z. Pan, D. Cuiuri, H. Li, A multi-bead overlapping model for robotic wire and arc additive manufacturing (WAAM), *Robotics and Computer-Integrated Manufacturing* 31 (2015) 101–110, doi:[10.1016/j.rcim.2014.08.008](https://doi.org/10.1016/j.rcim.2014.08.008).
- [10] J. Ding, P. Colegrove, J. Mehnen, S. Williams, F. Wang, P. Sequeira Almeida, A computationally efficient finite element model of wire and arc additive manufacturing, *The International Journal of Advanced Manufacturing Technology* 70 (2014) 227–236, doi:[10.1007/s00170-013-5261-x](https://doi.org/10.1007/s00170-013-5261-x).
- [11] X. Bai, H. Zhang, G. Wang, Improving prediction accuracy of thermal analysis for weld-based additive manufacturing by calibrating input parameters using IR imaging, *The International Journal of Advanced Manufacturing Technology* 69 (2013) 1087–1095, doi:[10.1007/s00170-013-5102-y](https://doi.org/10.1007/s00170-013-5102-y).
- [12] X. Bai, P. Colegrove, J. Ding, X. Zhou, C. Diao, P. Bridgeman, J. Hönnige, H. Zhang, S. Williams, Numerical analysis of heat transfer and fluid flow in multilayer deposition of PAW-based wire and arc additive manufacturing, *International Journal of Heat and Mass Transfer* 124 (2018) 504–516, doi:[10.1016/j.ijheatmasstransfer.2018.03.085](https://doi.org/10.1016/j.ijheatmasstransfer.2018.03.085).
- [13] Y. Ogino, S. Asai, Y. Hirata, Numerical simulation of WAAM process by a GMAW weld pool model, *Welding in the World* 62 (2) (2018) 393–401, doi:[10.1007/s40194-018-0556-z](https://doi.org/10.1007/s40194-018-0556-z).
- [14] X. Zhou, H. Zhang, G. Wang, X. Bai, Three-dimensional numerical simulation of arc and metal transport in arc welding based additive manufacturing, *International Journal of Heat and Mass Transfer* 103 (2016) 521–537, doi:[10.1016/j.ijheatmasstransfer.2016.06.084](https://doi.org/10.1016/j.ijheatmasstransfer.2016.06.084).
- [15] W. Ou, T. Mukherjee, G.L. Knapp, Y. Wei, T. DebRoy, Fusion zone geometries, cooling rates and solidification parameters during wire arc additive manufacturing, *International Journal of Heat and Mass Transfer* 127 (2018) 1084–1094, doi:[10.1016/j.ijheatmasstransfer.2018.08.111](https://doi.org/10.1016/j.ijheatmasstransfer.2018.08.111).
- [16] W. Zhang, C.H. Kim, T. DebRoy, Heat and fluid flow in complex joints during gas metal arc welding—Part I: numerical model of fillet welding, *Journal of Applied Physics* 95 (9) (2004) 5210–5219, doi:[10.1063/1.1699485](https://doi.org/10.1063/1.1699485).
- [17] S. Mishra, T. DebRoy, A heat-transfer and fluid-flow-based model to obtain a specific weld geometry using various combinations of welding variables, *Journal of Applied Physics* 98 (4) (2005) 044902, doi:[10.1063/1.2001153](https://doi.org/10.1063/1.2001153).

- [18] S. Kumar, S.C. Bhaduri, Three-dimensional finite element modeling of gas metal-arc welding, *Metallurgical and Materials Transactions B* 25 (3) (1994) 435–441, doi:[10.1007/BF02663394](https://doi.org/10.1007/BF02663394).
- [19] T. Mukherjee, H.L. Wei, A. De, T. DebRoy, Heat and fluid flow in additive manufacturing—Part I: Modeling of powder bed fusion, *Computational Materials Science* 150 (2018) 304–313, doi:[10.1016/j.commatsci.2018.04.022](https://doi.org/10.1016/j.commatsci.2018.04.022).
- [20] S.V. Patankar, *Numerical Heat Transfer and Fluid Flow*, McGraw-Hill, New York, 1982.
- [21] R.B. Bird, W.E. Stewart, E.N. Lightfoot, *Transport Phenomena, second ed.*, John Wiley & Sons, New York, 2002.
- [22] G.L. Knapp, T. Mukherjee, J.S. Zuback, H.L. Wei, T.A. Palmer, A. De, T. DebRoy, Building blocks for a digital twin of additive manufacturing, *Acta Materialia* 135 (2017) 390–399, doi:[10.1016/j.actamat.2017.06.039](https://doi.org/10.1016/j.actamat.2017.06.039).
- [23] V.R. Voller, C. Prakash, A fixed grid numerical modelling methodology for convection-diffusion mushy region phase-change problems, *International Journal of Heat and Mass Transfer* 30 (8) (1987) 1709–1719, doi:[10.1016/0017-9310\(87\)90317-6](https://doi.org/10.1016/0017-9310(87)90317-6).
- [24] A. De, T. DebRoy, A smart model to estimate effective thermal conductivity and viscosity in the weld pool, *Journal of Applied Physics* 95 (9) (2004) 5230–5240, doi:[10.1063/1.1695593](https://doi.org/10.1063/1.1695593).
- [25] A. Block-Bolten, T. Eagar, Metal vaporization from weld pools, *Metallurgical Transactions B* 15 (3) (1984) 461–469, doi:[10.1007/BF02657376](https://doi.org/10.1007/BF02657376).
- [26] Thermochemical data, in: E.A. Brandes, G.B. Brook (Eds.), *Smithells Metals Reference Book, seventh ed.*, Butterworth-Heinemann, Oxford, 1992, pp. 8–54.
- [27] M.V. Allmen, A. Blatter, in: *Laser-beam interactions with materials: physical principles and applications, 2*, Springer Science & Business Media, 2013, p. 116.
- [28] K. Mundra, T. DebRoy, Toward understanding alloying element vaporization during laser beam welding of stainless steel, *Welding Research* 72 (1) (1993) 1s–9s.
- [29] H.B. Smartt, *ASM Handbook*, ASM International, 1993, 27.
- [30] Z.N. Cao, P. Dong, Modeling of GMA weld pools with consideration of droplet impact, *Journal of Engineering Materials and Technology* 120 (4) (1998) 313–320, doi:[10.1115/1.2807020](https://doi.org/10.1115/1.2807020).
- [31] J. López, C. Zanzi, P. Gómez, R. Zamora, F. Faura, J. Hernández, An improved height function technique for computing interface curvature from volume fractions, *Computer Methods in Applied Mechanics and Engineering* 198 (33–36) (2009) 2555–2564, doi:[10.1016/j.cma.2009.03.007](https://doi.org/10.1016/j.cma.2009.03.007).
- [32] N. Patil, D. Pal, H.K. Rafi, K. Zeng, A. Moreland, A. Hicks, D. Beeler, B. Stucker, A generalized feed forward dynamic adaptive mesh refinement and derefinement finite element framework for metal laser sintering—Part I: formulation and algorithm development, *Journal of Manufacturing Science and Engineering* 137 (4) (2015) 041001, doi:[10.1115/1.4030059](https://doi.org/10.1115/1.4030059).
- [33] A. Ayed, A. Valencia, G. Bras, H. Bernard, P. Michaud, Y. Balcaen, J. Alexis, et al., Effects of WAAM process parameters on metallurgical and mechanical properties of Ti-6Al-4V deposits, in: F. Chaari, et al. (Eds.), *Advances in Materials, Mechanics and Manufacturing*, Springer, 2020, pp. 26–35, doi:[10.1007/978-3-030-24247-3_4](https://doi.org/10.1007/978-3-030-24247-3_4).
- [34] T. Mukherjee, V. Manvatkar, A. De, T. DebRoy, Dimensionless numbers in additive manufacturing, *Journal of Applied Physics* 121 (6) (2017) 064904, doi:[10.1063/1.4976006](https://doi.org/10.1063/1.4976006).
- [35] K.A. Jackson, Constitutional supercooling surface roughening, *Journal of Crystal Growth* 264 (4) (2004) 519–529, doi:[10.1016/j.jcrysgro.2003.12.074](https://doi.org/10.1016/j.jcrysgro.2003.12.074).
- [36] T. Mukherjee, H.L. Wei, A. De, T. DebRoy, Heat and fluid flow in additive manufacturing—Part II: powder bed fusion of stainless steel, and titanium, nickel and aluminum base alloys, *Computational Materials Science* 150 (2018) 369–380, doi:[10.1016/j.commatsci.2018.04.027](https://doi.org/10.1016/j.commatsci.2018.04.027).
- [37] K.C. Mills, Y. Su, Z. Li, R.F. Brooks, Equations for the calculation of the thermo-physical properties of stainless steel, *ISIJ international* 44 (10) (2004) 1661–1668, doi:[10.2355/isijinternational.44.1661](https://doi.org/10.2355/isijinternational.44.1661).
- [38] A. Kumar, T. DebRoy, Improving reliability of modelling heat and fluid flow in complex gas metal arc fillet welds—part II: application to welding of steel, *Journal of Physics D: Applied Physics* 38 (1) (2004) 127–134, doi:[10.1088/0022-3727/38/1/020](https://doi.org/10.1088/0022-3727/38/1/020).